

# Spontaneous Partial Order Driven by Intermolecular Interactions – Structure and Dynamics of Ice

Tianran Chen<sup>1\*</sup>, D. Jonathan P. Morris<sup>2</sup>, Anjana Samarakoon<sup>3</sup>,  
Isaac C. Ownby<sup>1</sup>, Arnab Banerjee<sup>3,7</sup>, Feng Ye<sup>3</sup>,  
Douglas L. Abernathy<sup>3</sup>, Zachary J. Morgan<sup>3</sup>, Joseph Lanier<sup>2,6</sup>,  
Konrad Siemensmeyer<sup>4</sup>, Bastian Klemke<sup>4</sup>, D. Alan Tennant<sup>1,5\*</sup>

<sup>1\*</sup>Department of Physics and Astronomy, University of Tennessee, 1408  
Circle Dr., Knoxville, 37996, TN, USA.

<sup>2</sup>Department of Physics and Engineering, Xavier University, 3800  
Victory Pkw., Cincinnati, 45207, OH, USA.

<sup>3</sup>Oak Ridge National Laboratory, 1 Bethel Valley Rd., Oak Ridge,  
37831, TN, USA.

<sup>4</sup>Helmholtz-Zentrum Berlin für Materialien und Energie,  
Hahn-Meitner-Platz 1, Berlin, 14109, Germany.

<sup>5</sup>Department of Materials Science and Engineering, University of  
Tennessee, 1001-1099 Estabrook Rd., Knoxville, 37996, TN, USA.

<sup>6</sup>Department of Physics, The Ohio State University, 191 West Woodruff  
Ave., Columbus, 43210, OH, USA.

<sup>7</sup>Department of Physics and Astronomy, Purdue University, 525  
Northwestern Ave., West Lafayette, 47906, IN, USA.

\*Corresponding author(s). E-mail(s): [tchen34@utk.edu](mailto:tchen34@utk.edu);  
[dtennant@utk.edu](mailto:dtennant@utk.edu);

Contributing authors: [morrisd3@xavier.edu](mailto:morrisd3@xavier.edu); [anjana8722@gmail.com](mailto:anjana8722@gmail.com);  
[iownby@vols.utk.edu](mailto:iownby@vols.utk.edu); [arnabb@purdue.edu](mailto:arnabb@purdue.edu); [yefl@ornl.gov](mailto:yefl@ornl.gov);  
[abernathydl@ornl.gov](mailto:abernathydl@ornl.gov); [morganzj@ornl.gov](mailto:morganzj@ornl.gov); [lanier.86@osu.edu](mailto:lanier.86@osu.edu);  
[siemensmeyer@helmholtz-berlin.de](mailto:siemensmeyer@helmholtz-berlin.de); [bastian.klemke@helmholtz-berlin.de](mailto:bastian.klemke@helmholtz-berlin.de);

## Abstract

Water ice’s remarkable properties make it an important material across a range of disciplines. The combination of covalent and hydrogen bonds form a long-range lattice of oxygens, which hosts a disordered yet correlated hydrogen network. We observe hidden strings of 1D order within the disordered manifold of hydrogen atoms – revealed via optical phonons within a large multi-dimensional neutron scattering dataset. Our analysis shows that nearest-neighbor intermolecular interactions drive partial ordering, rather than dipole interactions, and hints at a mechanism for ice Ih’s transition into ordered ice XI that may extend to other disordered phases. These insights have broader implications for non-periodic systems exhibiting local-symmetry, while enhancing our knowledge of lattice dynamics of this most intriguing material.

**Keywords:** ice Ih, neutron, phonon, partial order

## 1 Introduction

Water has fascinated artists, philosophers, and scientists throughout recorded history from Leonardo da Vinci to the modern scientist [1–3]. The highly unusual structural and dynamical properties of water ice have inspired intensive experimental, theoretical, and computational investigation for more than a century (e.g. [4–15]). At ambient pressure, water ice (Ih phase) has a hexagonal crystal structure, reflected geometrically in snowflakes [16]. The ordered oxygen lattice forms a disordered hydrogen network while obeying the Bernal-Fowler ice rules where (i) each oxygen-oxygen pair is separated by one hydrogen atom and (ii) each oxygen has two nearby hydrogen atoms and two faraway hydrogen atoms [5]. The hydrogen atoms in *pure* water ice are not observed to order at ambient pressure and low temperatures, although transitioning to the ordered XI phase is possible on geological timescales ( $\gtrsim 10,000$  years) [17]. Notably, ice Ih and XI exhibit significant differences in librational phonons (combination of rocking, wagging, and twisting motions of the water molecules) [18, 19]. In this study, we present neutron scattering measurements of single-crystal heavy water ice Ih ( $^2\text{H}_2\text{O}$ ) and provide novel theoretical insights into the correlations within the hydrogen network.

## Experimental Details

For neutron scattering experiments, heavy water ice ( $^2\text{H}_2\text{O}$ ) is preferred over light water ice ( $^1\text{H}_2\text{O}$ ), due to the lower incoherent scattering cross section of deuterium ( $^2\text{H}$ ) [20]. Single-crystal samples of  $^2\text{H}_2\text{O}$  ice Ih were prepared using a modified Bridgeman technique [15, 21].

Bragg and diffuse scattering were measured on the Elastic Diffuse Scattering Spectrometer (CORELLI, [22]), and complementary high-resolution inelastic neutron

scattering (INS) data were measured on the Wide Angular-Range Chopper Spectrometer (ARCS, [23]) both at the Spallation Neutron Source (SNS), Oak Ridge National Laboratory.

## Structure of Ice Ih

For computational simplicity, we use an orthogonal conventional unit cell with eight H<sub>2</sub>O molecules ( $a=4.3$  Å,  $b=7.71$  Å,  $c=7.27$  Å,  $\alpha=\beta=\gamma=90^\circ$ , CmCm space-group [24]). Fig.1a shows a typical ice Ih structure, comprising two types of oxygen atoms, O<sup>a</sup> and O<sup>b</sup> (Fig.1b). Each hydrogen atom bonds to one O<sup>a</sup> and one O<sup>b</sup>, displaced by 0.35 Å from the bond center [25, 26]. We use Ising variables ( $\sigma_i = +1$  or  $-1$ ) to represent whether a hydrogen is closer to O<sup>a</sup> or O<sup>b</sup> [27], and each oxygen's four bonds form a pseudospin four-vector  $\{\sigma_i\}$ .

We developed a novel algorithm to simulate hydrogen conformations in ice Ih (Supplementary Text), ensuring the ice rules are obeyed ( $\sum\sigma_i = 0$  for all oxygen sites). To better visualize these conformations, we color O<sup>a</sup>-O<sup>b</sup> bonds red or blue based on the Ising variable of the intervening hydrogen (Fig. 1c). The red and blue bonds form special chemical patterns [...-HOH-O-HOH-O-...], referred to as positive (+1) and negative (-1) Ising chains, respectively. While most chains are twisted, ice XI, which is thought to be the most stable conformation of ice Ih [28], exhibits armchair and zigzag Ising chains (Fig. 1d), which are the only quasi-1D forms possible in ice Ih.

Our calculated static structure factor, averaging over multiple  $4 \times 2 \times 2$  supercells with different hydrogen conformations (Fig. 1f), fits the elastic neutron data (Fig. 1e) reasonably well. However, the elastic neutron data can be better reproduced - specifically the sharp diffuse-scattering features - using alternative hydrogen conformations, explained in detail later.

## Dynamics of Ice Ih

### INS and Unconventional Librational Phonons

INS provides four-dimensional (4D) data in momentum transfer,  $\mathbf{Q} = H\mathbf{a}^* + K\mathbf{b}^* + L\mathbf{c}^*$ , and energy transfer,  $E$ . Fig.2a shows INS data integrated over three distinct energy ranges. We observed unconventional dispersive librational phonons along the  $L$ -axis (Fig. 2f). Four characteristic phonon frequencies were identified: the lattice modes upper-bound at  $\hbar\omega_1^{\text{exp}} = 39$  meV; the librational modes lower-bound at  $\hbar\omega_2^{\text{exp}} = 48$  meV; the intersections of dispersive librational modes at  $\hbar\omega_3^{\text{exp}} = 68$  meV; and the librational modes upper-bound at  $\hbar\omega_4^{\text{exp}} = 88$  meV. The high-frequency dispersive librational (HFDL) phonons in the 68–88 meV range are of particular interest because their occurrence is highly sensitive to hydrogen conformations, explained in detail later.

HFDL phonons are significantly weaker along the  $K$ -axis (Fig. 3j) compared to the  $L$ -axis (Fig. 3k). We measured INS while heating and cooling the sample between 3 and 240 K in 3 K steps. The temperature-dependent integrated intensities of HFDL phonons (see Supplementary Text and fig. 1),  $\rho_K(T)$  and  $\rho_L(T)$ , are plotted in Fig. 3a.  $\rho_L$  decreases by 70% as temperature increases from 1 K to 240 K, while  $\rho_K$  remains

consistently low. No temperature hysteresis is observed, indicating that the processes governing changes in HFDL phonon intensities equilibrate within the measurement timescale.

Sharp phonon peaks observed at 105 meV (Fig. 3j, k) are attributed to  $^1\text{H}_2\text{O}$  frost attached to the  $^2\text{H}_2\text{O}$  sample (Supplementary Text).

## Dynamic Model

To capture the local symmetry of ice Ih (Fig. 1b), we introduce 2-body stretching interactions  $U_b = \frac{1}{2}k_b(\Delta b)^2$ , where  $b$  represents the bonds OH, O-H, and O-O, and 3-body bending interactions  $U_\alpha = \frac{1}{2}k_\alpha(\Delta\alpha)^2$ , where  $\alpha$  represents the bond angles  $\angle\text{OH-O}$ ,  $\angle\text{HOH}$ ,  $\angle\text{HO-H}$ ,  $\angle\text{H-O-H}$ . Here, “-” denotes hydrogen bonds. These parameters ( $k_b$ ,  $k_\alpha$ ) are used to construct the force constant matrix  $\Phi$  which encodes the second derivatives of the potential energy with respect to atomic displacements for calculating phonon normal modes and frequencies (Supplementary Text). Similar terms have been previously used to model ice Ih dynamics but were constrained by limited datasets [29, 30].

To better understand phonon dynamics, we calculate the mean squared change (MSC) in bond lengths and angles for each mode [31]. The MSC of  $b$  and  $\alpha$  for the  $\nu$ -th  $\Gamma$ -phonon normal mode is given by  $D_b(\nu) = \frac{1}{N_b} \sum_{ij \in b} |\Delta r_{ij}(\nu)|^2$  and  $D_\alpha(\nu) = \frac{1}{N_\alpha} \sum_{\angle_{ijk} \in \alpha} r_{ji}r_{jk} |\Delta \angle_{ijk}(\nu)|^2$ . Here,  $\Delta r_{ij}(\nu)$  and  $\Delta \angle_{ijk}(\nu)$  represent the maximum change in bond length  $r_{ij}$  and angle  $\angle_{ijk}$  for the  $\nu$ -th  $\Gamma$ -phonon normal mode, respectively.  $N_b$  and  $N_\alpha$  are total number of bonds and angles belonging to  $b$  and  $\alpha$ .

As shown in Fig. 3b, the  $9n$   $\Gamma$ -phonon normal modes ( $n$  being the number of  $\text{H}_2\text{O}$  molecules) are categorized as lattice modes ( $\nu = 1$  to  $3n$ ), low-frequency librational (LFL) modes ( $\nu = 3n + 1$  to  $5n$ ), high-frequency librational (HFL) modes ( $\nu = 5n + 1$  to  $6n$ ), bending modes ( $\nu = 6n + 1$  to  $7n$ ), and stretching modes ( $\nu = 7n + 1$  to  $9n$ ). Theoretical values  $\omega_{3n}$ ,  $\omega_{3n+1}$ ,  $\omega_{5n}$ , and  $\omega_{6n}$  should match the experimental values  $\omega_1^{\text{exp}}$ ,  $\omega_2^{\text{exp}}$ ,  $\omega_3^{\text{exp}}$  and  $\omega_4^{\text{exp}}$  mentioned previously.

The force constants  $k_b$  and  $k_\alpha$ , having different dimensional units, are converted to effective frequencies  $\omega_b$  and  $\omega_\alpha$  using the relations  $\omega_b = \sqrt{\frac{k_b}{m_b^{\text{eff}}}}$  and  $\omega_\alpha = \sqrt{\frac{k_\alpha}{I_\alpha^{\text{eff}}}}$ , where  $m_{p=ij}^{\text{eff}} = \frac{m_i m_j}{m_i + m_j}$  is the effective reduced mass of  $b$ , and  $I_{\alpha=\angle_{ijk}}^{\text{eff}} = m_i r_{ij}^2 + m_k r_{jk}^2$  is the effective moment of inertia of  $\alpha$ . We obtained model parameters as  $\hbar(\omega_{\text{OH}}, \omega_{\text{OO}}, \omega_{\angle\text{OH-O}}, \omega_{\angle\text{HOH}}, \omega_{\angle\text{HO-H}}, \omega_{\angle\text{H-O-H}}) = (310, 26, 59, 150, 48, 66)$  meV to match the full neutron data ( $\omega_{\text{O-H}}$  is set to zero because it is correlated with  $\omega_{\text{OH}}$  and  $\omega_{\text{OO}}$ ; see Supplementary Text).

## Multiple-Phonon and One-phonon Processes

The 4D INS data (Fig. 2a) is a combination of multiple- and one-phonon processes. For example, Fig. 2d shows sharp acoustic-phonon features attributed to the one-phonon process and broad features around 6 meV associated with the multiple-phonon process. Our model successfully reproduces the INS patterns for both processes, employing separate formulas to effectively describe each (Supplementary Text).

Multiple-phonon processes in periodic systems are commonly treated as smooth backgrounds. However, in ice Ih, hydrogen disorder gives rise to distinctive patterns in  $\mathbf{Q}$ -space when integrated over energy. For example, the integration over 5–20 meV (Fig. 2b) is well reproduced by multiple-phonon DSF simulations using  $4 \times 2 \times 2$  supercells (Fig. 2c).

One-phonon DSF calculations using  $2 \times 1 \times 1$  supercells (Fig. 2e) closely match neutron data with incident energy  $E_i = 20$  meV (Fig. 2d). The calculated longitudinal and transverse acoustic phonon group velocities along  $L$  ( $v_g^l = 4.0$  km/s,  $v_g^t = 1.5$  km/s) agree with polycrystalline results ( $v_g^l = 3.8$  km/s,  $v_g^t = 1.8$  km/s) [32]. The simulation (Fig. 2g) also captures the unconventional dispersion of librational modes observed in neutron data with  $E_i = 150$  meV (Fig. 2f), though simulated intensities deviate from experimental values (see Supplementary Text for simulation details).

## Partial Order Beyond the Ice Rules

Our simulations using  $2 \times 1 \times 1$  supercells successfully reproduce HFDL modes (Fig. 2g), but the simulated intensities are much weaker than the low-frequency dispersive librational modes, scarcely reflecting experimental data. Increasing the supercell size to  $2 \times 1 \times 2$  fully suppresses HFDL phonons (Fig. 2h).

Fig. 3c shows the phonon band structure of the ice Ih conformation shown in Fig. 1c, displaying two HFDL bands along  $L$  but none along  $H$ . In contrast, Fig. 3d shows the phonon band structure of ice XI (Fig. 1d), which has four HFDL bands along both  $L$  and  $H$ . Remarkably, we found the number of HFDL phonon bands along  $L$  and  $H$  matches the count of armchair chains along  $[0, 0, 1]$  (Fig. 4f) and zigzag chains along  $[1, 0, 0]$  (Fig. 4e), respectively. Similarly, HFDL phonons along  $K$  correspond to the count of zigzag chains along directions  $[-\frac{1}{2}, \pm\frac{\sqrt{3}}{2}, 0]$ . Fig. 2i shows simulations using  $2 \times 1 \times 1$  supercells with higher armchair chain densities, resulting in strong HFDL phonon intensities that align closely with experimental data.

The HFL modes are primarily coupled bending modes of  $\angle\text{H-O-H}$  (Fig. 3b). HFDL phonon propagation requires that these  $\angle\text{H-O-H}$  are connected by stiffer  $\angle\text{HOH}$  angles rather than softer  $\angle\text{HO-H}$  angles, following a unique chemical pattern [...-HOH-O-HOH-O-...], i.e. the Ising chains. When HFL phonons propagate along quasi-1D Ising chains (armchair and zigzag chains), phonon energy and momentum are conserved along the chain. In contrast, at the vertices of twisted Ising chains, phonon energy and momentum are transferred to neighboring atoms, leading to the localization of HFL modes and resulting in flat phonon bands.

Our discovery of HFDL phonons along  $L$  indicates that ice Ih has much higher densities of armchair chains than are found in structural simulations constrained by ice rules alone, while zigzag chain densities remain low. Ice XI contains the maximum armchair and zigzag chains (Fig. 1d), suggesting those chains may have lower internal energies.

## Mechanism of the Partial Order Formation

The asymmetry of water molecules generates dipole moments within their symmetry planes, oriented toward the more positive hydrogen atoms. The total polarization of an armchair chain aligns along the chain, whereas in a zigzag chain, it is perpendicular (Fig. 4b). Lasave et al.'s Hamiltonian incorporates both the ice rules and dipole-dipole interactions, producing linear chains (or strings) of O-H bonds as Bjerrum defects ( $\text{OH}^+$ ) move through the ice-rule-obeying structure [33]. Strings could be a mechanism for the transition from ice Ih to ice IX [33], and might resemble Dirac strings in spin-ice, even showing similarities with the Kasteleyn transition [34, 35]. Despite this, our simulations using dipole interactions show no clear formation of armchair or zigzag chains (Supplementary Text and fig. 3B). Although armchair chains exhibit polarization, they are not unique in this regard. A large number of alternative conformations with same polarizations suppresses armchair chain formation under external or internal electric fields. This led us to consider alternative interactions, including nearest-neighbor intermolecular interactions (NNII), to explain the formation of partial order.

In ice Ih, hydrogen bonds connecting neighboring water molecules can be classified into six different types, determined by the relative orientations of the two water molecules. For a type- $n$  bond ( $n = 0-5$ ), the angle between the two water dipole moments projected perpendicular to the O-H bond is  $n\pi/3$  (Fig. 4a). Let  $N_h$  denote the total number of hydrogen bonds,  $\rho_n$  the fraction of type- $n$  bonds, and  $E_n$  their internal energy.  $E_n$  has been estimated using DFT[36] but not measured experimentally. Type-1 and type-5 bonds have equal energies, as do type-2 and type-4 bonds. The conformational entropy can be estimated as (Supplementary Text and fig. 4A):

$$S(\rho_0, \rho_3) \approx -N_h \left[ \rho_0 \ln(\rho_0) + \left(\frac{3}{4} - \rho_0\right) \ln\left(\frac{3}{8} - \frac{\rho_0}{2}\right) + \rho_3 \ln(\rho_3) + \left(\frac{1}{4} - \rho_3\right) \ln\left(\frac{1}{8} - \frac{\rho_3}{2}\right) \right]$$

The internal energy is:

$$U(\rho_0, \rho_3) = -N_h(\rho_0\Delta_0 + \rho_3\Delta_3)$$

where  $\Delta_0 = E_2 - E_0$  and  $\Delta_3 = E_1 - E_3$ .

The probability of the system in a given state is evaluated using Boltzmann distribution  $P(\rho_0, \rho_3; T) = \frac{1}{Z} e^{-F(\rho_0, \rho_3)/T}$  where  $Z = \int e^{-F(\rho_0, \rho_3)/T} d\rho_0 d\rho_3$  is the partition function and  $F(\rho_0, \rho_3) = U(\rho_0, \rho_3) - TS(\rho_0, \rho_3)$  is the Helmholtz free energy. The conformation map is divided into four quadrants centered at the highest entropy state with  $(\rho_0, \rho_3) = (1/4, 1/12)$  (Fig. 4c).

Each quadrant is associated with one minimum-entropy conformation: ice Ih<sup>I</sup>, Ih<sup>II</sup>, Ih<sup>III</sup>, and Ih<sup>IV</sup> with  $(\rho_0, \rho_3)$  equals  $(3/4, 1/4)$ ,  $(0, 1/4)$ ,  $(0, 0)$ , and  $(3/4, 0)$ , respectively (black dots in Fig. 4c). Only ice Ih<sup>I</sup> is fully ordered (zero entropy) with 50% armchair chains and 50% zigzag chains. The other three conformations exhibit some residual entropy resulting from symmetrically equivalent hydrogen bonds with  $E_1 = E_5$  and  $E_2 = E_4$ . Typical ordered Ising chains found within these conformations include arch chains in Ih<sup>II</sup>, spiral chains in Ih<sup>III</sup>, and step chains in Ih<sup>IV</sup> (Fig. 4c).

However, only armchair chains reproduce the experimentally observed HFDL phonons along  $L$  (see Supplementary Text and fig. 3B). The four conformations are most stable when the signs of  $(\Delta_0, \Delta_3)$  are  $(+, +)$ ,  $(-, +)$ ,  $(-, -)$ , and  $(+, -)$  for  $\text{Ih}^I$ ,  $\text{Ih}^{II}$ ,  $\text{Ih}^{III}$ , and  $\text{Ih}^{IV}$ , respectively.

Ice  $\text{Ih}^I$  corresponds to ice XI. Fig. 4c shows  $P(\rho_0, \rho_3; T)$  for five  $(\Delta_0, \Delta_3)$  configurations: (1) (50, 200) K, (1') (100, 25) K, (2) (-50, 200) K, (3) (-50, -200) K, and (4) (50, -200) K, at  $T = +\infty, 240, 120, 80, 50$  and 30 K. We use simulated annealing (Supplementary Text) to model the cooling process from 300 K to 1 K for each configuration. The results (Fig. 4e) are plotted in the  $(\rho_0, \rho_3)$  plane and color-coded by temperature. At high temperatures, the system aligns with Boltzmann statistics, but at low temperatures, it becomes trapped in some local energy minima. Fig. 4g illustrates one such structure for configuration (1), where two ice XI domains with highlighted armchair chains are present. The red and blue armchair Ising chains have opposite polarizations, and the large energy barrier to flipping an entire domain inhibits full ordering. The anisotropic domain sizes, being much longer in the  $c$ -direction but shorter in the  $ab$  plane, result in significantly shorter average zigzag chain lengths compared to armchair chains.

Fig. 4d shows the Boltzmann distributions of zigzag and armchair chain densities,  $\rho_z$  and  $\rho_a$ , which are linear combinations of  $\rho_0$  and  $\rho_3$  (Supplementary Text). Fig. 4f presents the simulated annealing results for configurations (1) and (1'). The trends in  $\rho_a(T)$  for configuration (1) match the experimental intensities  $\rho_L(T)$  in Fig. 3a, supporting the condition  $\Delta_3 > \Delta_0 > 0$ .  $\rho_z(T)$  increases rapidly at low temperatures but  $\rho_K(T)$  does not. We note that  $\rho_K(T)$  is not only proportional to  $\rho_z(T)$  but also depends on the average length of zigzag chains. The low-temperature discrepancy between  $\rho_z(T)$  and  $\rho_K(T)$  likely arises from the much shorter average length of zigzag chains confined within anisotropic domains, which suppresses the HFDL phonon intensities along  $K$ .

The six types of hydrogen bonds have different pair distributions, indicating conformations with different  $\rho_0$  and  $\rho_3$  yield different elastic diffuse scattering patterns. Conformations with higher  $\rho_3$  and therefore higher armchair chain density (Fig. 1g) better reproduce the data (Fig. 1e), displaying anisotropic peaks that are broader along  $K$ —a feature absent in conventional simulations (Fig. 1f) or those with higher  $\rho_0$  (Fig. 1h).

This NNII-driven partial ordering mechanism could extend beyond academic interest in ice Ih, potentially influencing the growth and structure of ice crystals and snowflakes. Temperature and saturation ratios affect ice crystal formation, determining whether growth favors vertical columnar structures or horizontal plate-like forms [37].  $\Delta_0$  and  $\Delta_3$  may vary with environmental conditions, favoring columnar ice crystals when  $\Delta_3 > \Delta_0$  and plate-like crystals when  $\Delta_3 < \Delta_0$ . Additionally, this mechanism predicts that ice becomes more ordered under compression, where intermolecular distances shorten and both  $\Delta_0$  and  $\Delta_3$  increase. This mechanism could apply to other hydrogen-disordered ice phases. For instance, partial ordering driven by NNII upon cooling in cubic ice (ice Ic) could yield a fully ordered phase consisting of 100% zigzag chains. A hydrogen-ordered conformation of cubic ice, termed ice XIc, has been proposed [38, 39].

## Conclusion

Water ice is the quintessential example of a disordered crystal. Its hexagonal lattice of oxygen atoms hosts a tangled network of hydrogen bonds constrained by the ice rules. Long-range correlations within this network have been previously revealed by pinch-points in diffuse neutron scattering [8, 13].

Probing single-crystal water ice with complementary neutron scattering techniques allows for the development of a robust model that effectively captures the local symmetry of ice Ih. The resulting model has minimal parameters that accurately describes the entire 4D datasets.

Our high-quality dataset adds to the canon of literature supporting the application of the ice-rules to ice Ih, whilst capturing sufficient detail of its structure and dynamics to reveal unexpected chain motifs throughout the hydrogen network. We observed dispersive librational phonons which provide evidence of partial order, manifesting as armchair and zigzag chains. Furthermore, experimental measurements indicate that the degree of partial order increases upon cooling, offering new insights into the ordering processes in ice Ih.

We proposed a mechanism that the formation of partial order is driven by intermolecular interactions. High temperatures correspond to the highest-entropy state, while cooling favors emergence of partial order, particularly armchair chains because of their lower internal energy. Our model predicts that ice XI is achieved at zero temperature, but simulations show domain trapping at low temperatures, consistent with the slow natural transition to ice XI. These results offer a new perspective on the structure and dynamics of ice phases which could shed light on many aspects of ice science from structural phase transitions to the geometry of snowflakes.

## References

- [1] Pfister, L., Savenije, H.H.G., Fenicia, F.: Leonardo da Vinci’s Water Theory: on the Origin and Fate of Water. IAHS Press, Wallingford, Oxfordshire, UK (2009)
- [2] Artemov, V.: A historical review of the structure of water and ice. In: The Electrodynamics of Water and Ice, vol. 124, pp. 1–49. Springer, Switzerland (2021)
- [3] Finney, J.L.: The structure of water: a historical perspective. *J. Chem. Phys.* **160**, 060901 (2024)
- [4] Barnes, W.H.: The structure of ice between 0°C, and -183°C. *Proc. Royal Soc. A* **125**, 670–693 (1929)
- [5] Bernal, J.D., Fowler, R.H.: A theory of water and ionic solution, with particular reference to hydrogen and hydroxyl ions. *J. Chem. Phys.* **1**, 515–548 (1933)
- [6] Rahman, A., Stillinger, F.H.: Proton distribution in ice and the Kirkwood correlation factor. *J. Chem. Phys.* **57**, 4009–4017 (1972)

- [7] Li, J., Ross, D.K.: Evidence of two kinds of hydrogen bond in ice. *Nature* **365**, 327–329 (1993)
- [8] Li, J.C., Nield, V.M., Ross, D.K., Whitworth, R.W., Wilson, C.C., Keen, D.A.: Diffuse neutron-scattering of deuterated ice Ih. *Phil. Mag. B* **69**, 1173–1181 (1994)
- [9] Cowin, J.P., Tsekouras, A.A., Iedema, M.J., Wu, K., Ellison, G.B.: Immobility of protons in ice from 30 to 190 K. *Nature* **398**, 405–407 (1999)
- [10] Rick, S.W., Haymet, A.D.J.: Dielectric constant and proton order and disorder in ice Ih: Monte Carlo computer simulations. *J. Chem. Phys.* **118**, 9291–9296 (2003)
- [11] Buch, V., Groenzin, H., Li, I., Shultz, M.J., Tosatti, E.: Proton order in the ice crystal surface. *PNAS* **105**, 5969–5974 (2008)
- [12] Bove, L.E., Klotz, S., Paciaroni, A., Sacchetti, F.: Anomalous proton dynamics in ice at low temperatures. *Phys. Rev. Lett.* **103**, 165901 (2009)
- [13] Isakov, S.V., Moessner, R., Sondhi, S.L., Tennant, D.A.: Analytical theory for proton correlations in common-water ice Ih. *Phys Rev. B* **91**, 245152 (2015)
- [14] Drechsel-Grau, C., Marx, D.: Collective proton transfer in ordinary ice: local environments, temperature dependence and deuteration effects. *Phys. Chem. Chem. Phys.* **19**, 2623 (2017)
- [15] Morris, D.J.P., Siemsmeyer, K., Hoffman, J.-U., Klemke, B., Glavatski, K., Seiffert, K., Tennant, D.A., Isakov, S.V., Sondhi, S.V., Moessner, R.: Neutron studies of gauge field and charge in Ih heavy-water ice. *Phys. Rev. B* **99**, 174111 (2019)
- [16] Libbrecht, K.G.: The physics of snow crystals. *Rep. Prog. Phys.* **68**, 855–895 (2005)
- [17] Fukazawa, H., Hoshikawa, A., Ishi, Y., Chakoumakos, B.C., Fernandez-Baca, J.A.: Existence of ferroelectric ice in the universe. *Astrophys. J.* **652**, 57–60 (2006)
- [18] Erba, A., Casassa, S., Dovesi, R., Maschio, L., Pisani, C.: Periodic density functional theory and local-MP2 study of the librational modes of ice XI. *J. Chem. Phys.* **130**(7), 074505 (2009)
- [19] Li, J.-C., Nield, V.M., Jackson, S.M.: Spectroscopic measurements of ice XI. *Chem. Phys. Lett.* **241**, 290–294 (1995)
- [20] Sears, V.F.: Neutron scattering lengths and cross sections. *Neutron News* **3**, 26–37 (1992)
- [21] Ohtomo, M., Ahmad, S., Whitworth, R.W.: A technique for the growth of high

- quality single crystals of ice. *J. Phys. Colloques* **48 C1**, 595–598 (1987)
- [22] Rosenkranz, S., Osborn, R.: Corelli: efficient single crystal diffraction with elastic discrimination. *PRAMANA* **71**, 705–711 (2008)
- [23] Abernathy, D.L., Stone, M.B., Loguillo, M.J., Lucas, M.S., Delaire, O., Tang, X., Lin, J.Y.Y., Fultz, B.: Design and operation of the wide angular-range chopper spectrometer ARCS at the Spallation Neutron Source. *Rev. Sci. Instrum.* **83**, 015114 (2012)
- [24] Hayward, J.A., Reimers, J.R.: Unit cells for the simulation of hexagonal ice. *J. Chem. Phys.* **106**, 1518–1529 (1997)
- [25] Bergmann, U., Di Cicco, A., Wernet, P., Principi, E., Glatzel, P., Nilsson, A.: Nearest-neighbor oxygen distances in liquid water and ice observed by x-ray Raman based extended x-ray absorption fine structure. *J Chem. Phys.* **127**(17), 174504 (2007)
- [26] Pedersen, A., Karssemeijer, L., Cuppen, H.M., Jónsson, H.: Long-timescale simulations of H<sub>2</sub>O admolecule diffusion on ice Ih(0001) surfaces. *J. Phys. Chem. C* **119**, 16528–16536 (2015)
- [27] Rzyhkin, I.A.: Frustration model of proton disorder in ice. *Solid State Comm.* **52**, 49–52 (1984)
- [28] Fan, X., Bing, D., Zhang, J., Shen, Z., Kuo, J.-L.: Predicting the hydrogen bond ordered structures of ice ih, ii, iii, vi and ice vii: Dft methods with localized based set. *Computational Materials Science* **49**(4), 170–175 (2010)
- [29] Mitzdorf, U., Helmreich, D.: Elastic constants of D<sub>2</sub>O ice and variation of intermolecular forces on deuteration. *J. Acoustical Soc. Amer.* **49**, 723–728 (1969)
- [30] Li, J.C., Ross, D.K.: Inelastic neutron scattering studies of defect modes of h in d<sub>2</sub>o ice ih. *Journal of Physics: Condensed Matter* **6**(49), 10823 (1994)
- [31] Dove, M.T.: *Introduction to Lattice Dynamics*. Cambridge University Press, Cambridge (1993)
- [32] Vogt, C., Laihem, K., Wiebusch, C.: Speed of sound in bubble-free ice. *J. Acoust. Soc. Am.* **124**, 3613–3618 (2008)
- [33] Lasave, S., Koval, S., Laio, A., Tosatti, E.: Proton strings and rings in atypical nucleation of ferroelectricity in ice. *PNAS* **118**, 2018837118 (2020)
- [34] Kasteleyn, P.W.: Dimer statistics and phase transitions. *J. Math. Phys.* **4**, 287 (1963)

- [35] Jaubert, L.D.C., Chalker, J.T., Holdsworth, P.C.W., Moessner, R.: Three-dimensional kasteleyn transition: spin ice in a [100] field. *Physical Review Letters* **100**(6), 067207 (2008)
- [36] Baranyai, A., Bartók, A., Chialvo, A.A.: Computer simulation of the 13 crystalline phases of ice. *The Journal of chemical physics* **123**(5) (2005)
- [37] Nakaya, U.: *Snow Crystals: Natural and Artificial*. Harvard University Press, ??? (1954)
- [38] Raza, Z., Alfe, D., Salzmann, C.G., Klimeš, J., Michaelides, A., Slater, B.: Proton ordering in cubic ice and hexagonal ice; a potential new ice phase—xic. *Physical Chemistry Chemical Physics* **13**(44), 19788–19795 (2011)
- [39] Geiger, P., Dellago, C., Macher, M., Franchini, C., Kresse, G., Bernard, J., Stern, J.N., Loerting, T.: Proton ordering of cubic ice ic: Spectroscopy and computer simulations. *The Journal of Physical Chemistry C* **118**(20), 10989–10997 (2014)
- [40] Ramirez-Cuesta, A.J., Jones, M.O., David, W.I.F.: Neutron scattering and hydrogen storage. *Materials Today* **12**, 54–61 (2009)
- [41] Squires, G.L.: *Introduction to the Theory of Thermal Neutron Scattering*. Cambridge University Press, Cambridge (1978)
- [42] Willis, B.T.M., Carlile, C.J.: *Experimental Neutron Scattering*. Oxford University Press, Oxford (2009)
- [43] Lin, J.Y.Y., Banerjee, A., Islam, F., Le, M.D., Abernathy, D.L.: Energy dependence of the flux and elastic resolution for the ARCS neutron spectrometer. *Physica B: Cond. Matter* **562**, 26–30 (2019)
- [44] De Marco, L., Carpenter, W., Liu, H., Biswas, R., Bowman, J.M., Tokmakoff, A.: Differences in the vibrational dynamics of  $\text{H}_2\text{O}$  and  $\text{D}_2\text{O}$ : Observation of symmetric and antisymmetric stretching vibrations in heavy water. *The Journal of Physical Chemistry Letters* **7**(10), 1769–1774 (2016)
- [45] Cote, A.S., Morrison, I., Cui, X., Jenkins, S., Ross, D.K.: Ab-initio density-functional lattice-dynamics studies of ice. *Can. J. Phys.* **81**, 115–122 (2003)
- [46] Adeagbo, W.A., Entel, P.: Influence of dipole interactions on the lattice dynamics of crystalline ice. *Phase Transitions* **78**, 799–810 (2005)
- [47] Rego, J.S., Konig, M.: Density-functional theory prediction of the elastic constants of ice Ih. *J. Chem. Phys.* **152**, 084502 (2020)

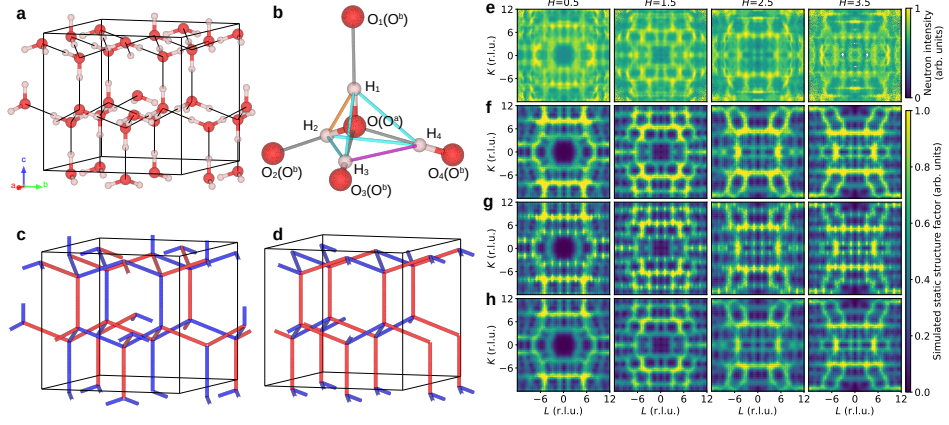


**Fig. 1 Structure and elastic neutron scattering of ice Ih.** (a) A  $2 \times 1 \times 1$  supercell of ice Ih. (b) Local geometry of ice Ih with an Ising configuration  $\{\sigma_i\} = (+1, +1, -1, -1)$ . (c, d) Ising chain conformations in (c) the ice Ih structure shown in (a) and (d) ice XI, where positive and negative Ising chains are shown in red and blue, respectively. (e) Experimental elastic neutron scattering data taken at  $T=1$  K, sliced along  $K$  and  $L$  for  $H=0.5, 1.5, 2.5, 3.5$  (r.l.u.). (f-h) Simulated elastic neutron scattering data using  $4 \times 2 \times 2$  supercells with different hydrogen configurations: (f) conventional conformations obeying the ice rules, (g) conformations with a higher density of type-3 hydrogen bonds ( $\rho_3$ ), and (h) conformations with a higher density of type-0 hydrogen bonds ( $\rho_0$ ). Both experimental data and simulations are divided by the Debye-Waller factor to enhance high- $Q$  features.

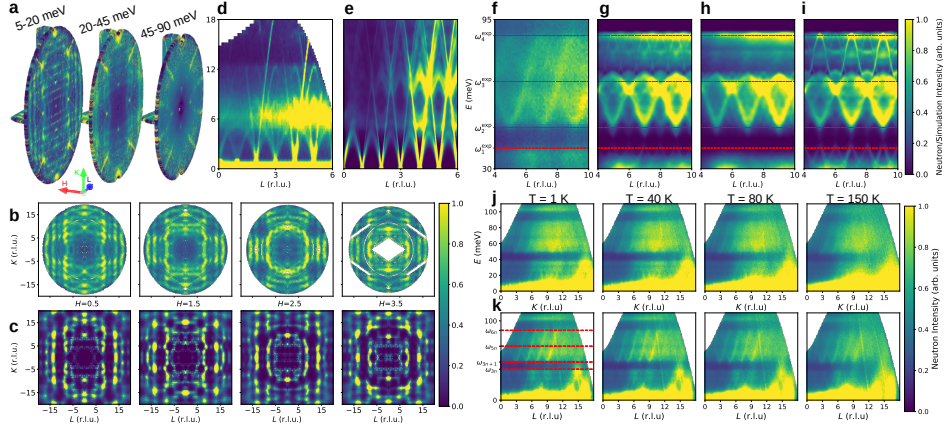


**Fig. 2** INS data and simulations of ice Ih. (a) 4D INS data taken at 1 K, integrated over different energy ranges. (b) Inelastic scattering data sliced along  $K$  and  $L$  for  $H=0.5, 1.5, 2.5, 3.5$  (r.l.u.) with  $E$  integrated over 5-20 meV. (c) Corresponding multiple-phonon process simulations using  $4 \times 2 \times 2$  supercells. (d) INS data with incident neutron energy  $E_i = 20$  meV, sliced along  $L$  and  $E$ , with  $H$  and  $K$  integrated over 0-0.1, 0.9-1.1, 1.9-2.1 (r.l.u.). The broad feature around 6 meV arises from the multiple-phonon process. (e) Corresponding one-phonon process simulations using  $2 \times 1 \times 1$  supercells. (f) INS data with  $E_i = 150$  meV sliced along  $L$  and  $E$ , with  $H$  and  $K$  integrated over 0-2 r.l.u. (g-i) Corresponding one-phonon process simulations using (g)  $2 \times 1 \times 1$  supercells, (h)  $2 \times 1 \times 2$  supercells, (i)  $2 \times 1 \times 1$  supercells with a high density of armchair chains. (j, k) INS data at 1, 40, 80, and 150 K along (j)  $K$  and (k)  $H$ , integrated over (j)  $H, L = 0-2$  r.l.u. and (k)  $K, L = 0-2$  r.l.u.

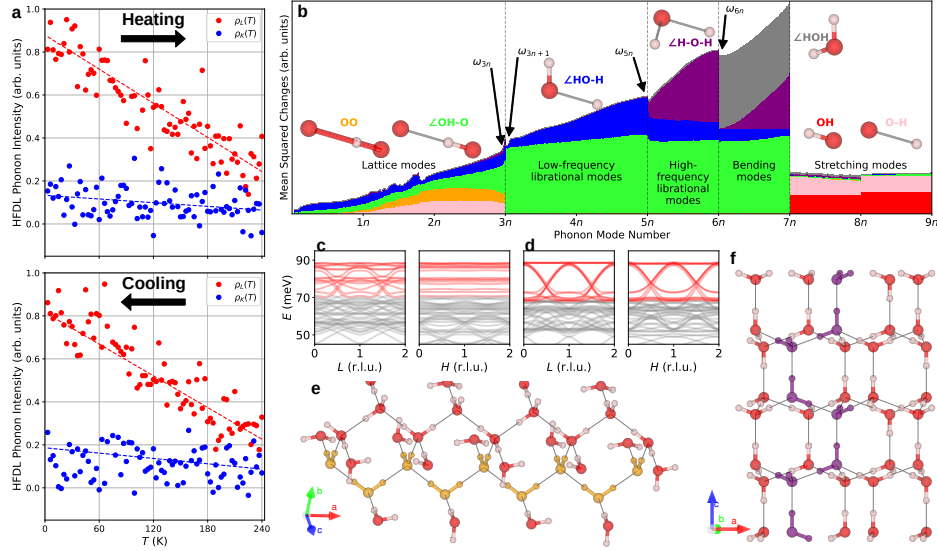


**Fig. 3 Phonon mode analysis and librational phonon band structures.** (a) HFDL phonon intensities along  $K$  and  $L$  at different temperatures upon heating and cooling. Dashed lines are guides to the eye. (b) MSC in bond lengths and angles for all  $\Gamma$ -phonon normal modes, plotted as a function of mode number  $\nu$ . Bonds and angles are color-coded: OH (red), O-H (pink), OO (orange),  $\angle OH-O$  (green),  $\angle HOH$  (grey),  $\angle HO-H$  (blue), and  $\angle H-O-H$  (purple). (c) Librational phonon band structures along  $L$  and  $H$  for the ice Ih conformation in Fig. 1 (c), containing 2 and 0 HFDL bands, respectively. (d) Librational phonon band structures along  $L$  and  $H$  for ice XI in Fig. 1 (d), both containing 4 HFDL bands. LFL modes are shown in grey, HFL modes in red. (e, f) Crystal structures highlighting (e) the zigzag chain (orange) along  $a$ -axis, and (f) the armchair chain (purple) along  $c$ -axis.

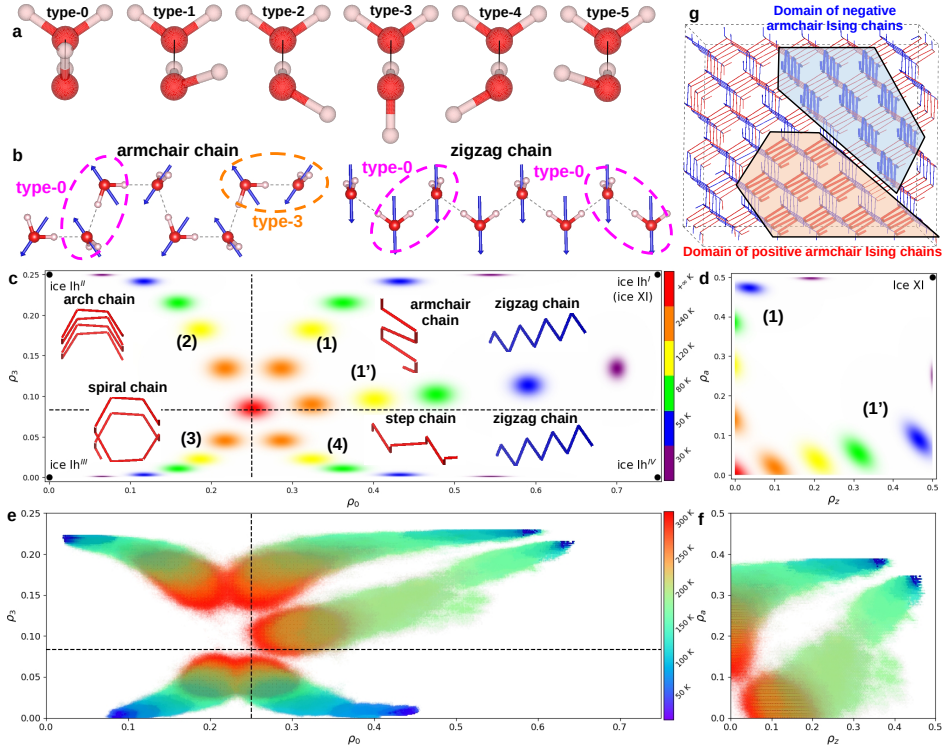


**Fig. 4 Partial order driven by NNII.** (a) The six hydrogen bond types connecting water molecule pairs in ice Ih. (b) Chain structures in ice Ih: armchair chains with 50% type-0 (magenta) and 50% type-3 (orange) bonds, and zigzag chains with all type-0 bonds. Water dipole moments are shown by blue arrows. (c) Conformation map of ice Ih in  $(\rho_0, \rho_3)$  coordinates, divided by dashed lines representing maximum-entropy  $\rho_0$  and  $\rho_3$  into four quadrants. Minimum-entropy conformations are marked as black dots at each corner, with corresponding Ising chain structures depicted. Boltzmann distributions are presented at temperatures  $+\infty$ , 240, 120, 80, 50, and 30 K for five configurations of  $(\Delta_0, \Delta_3)$ : (1) (50, 200) K; (1') (100, 25) K; (2) (-50, 200) K; (3) (-50, -200) K; and (4) (50, -200) K. (d) Boltzmann distributions of (1) and (1') in  $(\rho_z, \rho_a)$  coordinates. (e) Simulated annealing results for a  $6 \times 3 \times 3$  supercell cooled from 300 K to 1 K, using the five configurations. (f) Simulated annealing results for (1) and (1') in  $(\rho_z, \rho_a)$  coordinates. (g) Typical final structure at 1 K with (1) configuration. Positive and negative Ising chains are shown in red and blue. Armchair chains are highlighted to show two ice XI domains with opposite polarizations.

# Materials and Methods

## Sample Preparation

Pure water Ice Ih can be problematic for neutron scattering experiments as hydrogen ( $^1\text{H}$ ) nuclei scatter neutrons incoherently and increase the background counts (e.g. [40]). Therefore we used heavy water ( $^2\text{H}_2\text{O}$ ) because deuterium produces much less incoherent scattering, hence less background scattering in the data [20].

High quality single-crystal samples were prepared at the Helmholtz-Zentrum Berlin by a modified Bridgeman technique based on Ohtomo et al. [21]. Liquid heavy water was placed into a growth cell made up of a 1 cm diameter silicone-rubber tube which terminated in a narrow plastic spiral. Below the cell was a bath of ethylene glycol in water in a ratio of 23:73 kept at a temperature  $<2^\circ\text{C}$  by a Julabo refrigeration circulator. Just above the surface of the ethylene glycol solution was a circular heating element designed to keep a large temperature gradient from above freezing to below freezing as we lowered the cell into the solution. The entire set up was kept in a cold room kept between  $6^\circ\text{C}$  and  $10^\circ\text{C}$ , and  $^2\text{H}_2\text{O}$  in the sample cell was degassed by pumping with a vacuum pump. The sample cell was lowered in a controlled way into the solution via a stepper motor. As crystallites formed in the lowest portion of the cell the change in direction of the spiral meant that ideally one crystallite grows into the cylindrical portion of the growth cell. It took approximately 1 week to produce a 12 cm long crystal. The crystal was removed by cutting the tubing and cleaved. Birefringence was used to screen samples for obvious multiple crystallites.

## Neutron Scattering

Elastic neutron scattering measurements were performed on the Elastic Diffuse Scattering Spectrometer (CORELLI) at the Spallation Neutron Source (SNS) at Oak Ridge National Laboratory (ORNL) [22]. Detectors covering a solid angle of 2 steradians utilize time-of-flight neutrons to measure elastic and INS; a cross-correlation chopper then allows for the discrimination of elastic scattering from inelastic scattering. Data was collected for 2 or 4 minutes per angle and the sample was rotated by  $3^\circ$  over a range of  $180\text{-}360^\circ$ , and at temperatures of 1-200 K.

The sample was kept cold in a top-loading Orange Cryostat with Helium-3 insert with 300 mb pressure of Helium to avoid sublimation.

We performed elastic neutron scattering measurements on a single-crystal  $^2\text{H}_2\text{O}$  ice Ih sample and observed sharp Bragg peaks at integer indices, indicating high crystal quality. The scattering patterns can be well simulated by the coherent static structure factor (SSF) formula [41, 42]:

$$S(\mathbf{Q}) = N e^{-\langle|\mathbf{Q}\cdot\mathbf{u}|^2\rangle} \left| \sum_i \bar{b}_i e^{i\mathbf{Q}\cdot\mathbf{r}_i} \right|^2,$$

where  $N$  is the number of atoms, the summation is over each atom  $j$ ,  $e^{-\langle|\mathbf{Q}\cdot\mathbf{u}_j|^2\rangle}$  is the Debye-Waller factor where  $\mathbf{Q}$  is the reciprocal lattice vector (momentum transfer) and  $\mathbf{u}$  is the average atomic displacement,  $\bar{b}_\text{O} = 5.803$  fm and  $\bar{b}_\text{D} = 6.671$  fm are

the neutron coherent scattering lengths [20], and  $\mathbf{r}_j$  is the average atomic position. Simulations using larger supercells up to  $8 \times 4 \times 4$  show negligible difference from the  $4 \times 2 \times 2$  results.

Complementary high-resolution INS data were measured on the Wide Angular Range Chopper Spectrometer (ARCS) at the SNS [23]. The phonon dispersions used the high-resolution Fermi Chopper “ARCS-100-1.5” spinning at 420 Hz, providing a native resolution of 4% of  $E_i$  at the elastic line, with specifications and native energy resolutions available in the literature [43]. The initial energy of the neutrons is determined by the chopper settings and was set to 20 meV (Fermi chopper frequency 420 Hz,  $T_0$  chopper 60 Hz), 60 meV (Fermi chopper frequency 420 Hz,  $T_0$  chopper 120 Hz), 150 meV (Fermi chopper frequency 420 Hz,  $T_0$  chopper 120 Hz), 350 meV and 400 meV (Fermi chopper frequency 600 Hz,  $T_0$  chopper 120 Hz, with a phase shift distinguishing between the two energies) to provide sensitivity to a range of energy transfers. During the measurement, the sample was rotated by  $2^\circ$  every 4 minutes.

Prior to the experiment the sample was stored in a  $-80^\circ\text{C}$  freezer and then brought to the CORELLI beamline in a container of dry ice. Prior to inserting the sample the cryostat was set to 190K and purged with helium gas in order to avoid condensation while the variable temperature sample stick was removed and the ice sample quickly screwed into position. The sample holder was wrapped in cadmium to reduce background scattering. The sample stick was then placed back into the cold cryostat. Measurements were performed between 1-200 K (on CORELLI) with a 300 mb pressure of Helium to reduce the risk of sublimation of the sample. After the CORELLI experiment the cold cryostat containing the mounted sample was moved via crane and cart from the CORELLI to the ARCS instruments where it was inserted into the instrument for the inelastic measurements. After the ARCS experiment the sample was removed, stored in a container of dry ice in the  $-80^\circ\text{C}$  freezer.

## Supplementary Text

### A Novel Algorithm to Simulate Hydrogen Conformation

We introduce a novel algorithm to simulate the hydrogen conformation in ice Ih obeying to the ice rules. Each oxygen atom (take  $O^a$  for example) and its four surrounding hydrogen atoms have 16 possible Ising configurations (two configuration with all hydrogen either close to/far from the oxygen giving  $\Sigma\sigma_i = \pm 4$ ; eight configurations with three hydrogen either close to / far from the oxygen giving  $\Sigma\sigma_i = \pm 2$ ; six configurations obey the ice-rules and have two hydrogen close to the oxygen and two hydrogen far away giving  $\Sigma\sigma_i = 0$ ). The signs would be reversed for  $O^b$ . The 6 configurations that conform to the ice-rules are labeled as  $\mathbf{s}_1, \dots, \mathbf{s}_6$  where each  $\mathbf{s}_i$  is a pseudospin four-vector. Fig. 1b shows configuration  $\mathbf{s}_1 = (+1, +1, -1, -1)$ , where the central oxygen forms two covalent bonds with those closest hydrogen atoms (labeled  $H_1$  and  $H_2$ ), and two hydrogen bonds with the two furthest hydrogen atoms (labeled  $H_3$  and  $H_4$ ). In order to create the initial ice structure computationally we initialize the Ising configurations randomly and sweep over the oxygen sites in a random sequence. For each oxygen with Ising four-vector  $\mathbf{s}$ , we compute the inner products  $\mathbf{s} \cdot \mathbf{s}_i$  and replace  $\mathbf{s}$

with the  $\mathbf{s}_i$  that maximizes the inner product. If multiple  $\mathbf{s}_i$  maximize the inner product, we randomly select one. This process is repeated until all configurations obey the ice rules. Periodic boundary conditions are applied in the simulation.

## Quantitative Analysis of HF DL Phonon Intensities in Neutron Scattering Data

Fig. 1A displays the inelastic neutron intensities  $I(L, E)$  at 1 K, sliced along  $L$  and  $E$ , obtained by integrating the 4D intensities  $I(H, K, L, E)$  over  $H$  and  $K$  for  $L$  in the range 0-4 r.l.u. The high- and low-frequency dispersive librational phonons are well described by cosine functions,  $68 \pm 20 \cos(\frac{\pi}{2}L)$  meV, shown as red and blue dashed lines in fig. 1A.

To extract 1D intensity profiles  $I(L)$  from the 2D map  $I(L, E)$ , we applied a convolution method:

$$I(L_0) = \int \int I(L, E) C(L_0 - L, E) dE dL$$

where  $C(L, E)$  is a cosine-shaped kernel, illustrated in orange in fig. 1A:

$$C(L, E) = \begin{cases} 1, & \text{if } E = 68 + 20 \cos(\frac{\pi}{2}L) \text{ (meV) and } |L| \leq 1 \text{ (r.l.u.)}, \\ 0, & \text{otherwise.} \end{cases}$$

A Gaussian smoothing of variance  $\sigma = 1.7$  meV is applied to the kernel. To quantify the HF DL phonon intensities, we computed:

$$\rho_L = \int [I(L) - \overline{I(L)}] \cos(L\pi + \pi) dL$$

where  $\cos(L\pi + \pi)$  isolates HF DL phonon peaks observed at  $L = 3, 5, 7, 9, 11$  (r.l.u.).

Finally, note that all formulas for  $L$  can be equivalently adapted for  $K$ . Fig. 1B shows  $I(K)$  and  $I(L)$  at 1, 40, 80, and 150 K, while  $\rho_L$  and  $\rho_K$  at different temperatures are shown in Fig. 3a.

## Anomalous Phonon Modes at 105 meV

The phonon band at 105 meV (Fig. 3) observed in our measurements does not align with the simulated phonon dispersions for  $^2\text{H}_2\text{O}$ . This anomalous feature, likely absent in pure heavy ice Ih, may originate from  $^1\text{H}$  defects [30]. The large incoherent scattering cross section of  $^1\text{H}$  makes its detection straightforward in neutron scattering experiments, even in small quantities [44]. Both  $^1\text{H}_2\text{O}$  and  $^1\text{HO}^2\text{H}$  impurities in  $^2\text{H}_2\text{O}$  ice Ih introduce librational modes at 105 meV [30]. Additionally, the bending modes of  $^1\text{H}_2\text{O}$  are at 200 meV, while the bending modes of  $^1\text{HO}^2\text{H}$  are at 185 meV [30].

To identify the source of the impurities, we conducted additional measurements with an incident energy of 400 meV (fig. 2A). The integrated neutron scattering intensities, shown in fig. 2B, revealed two prominent peaks at 150 and 200 meV, which can

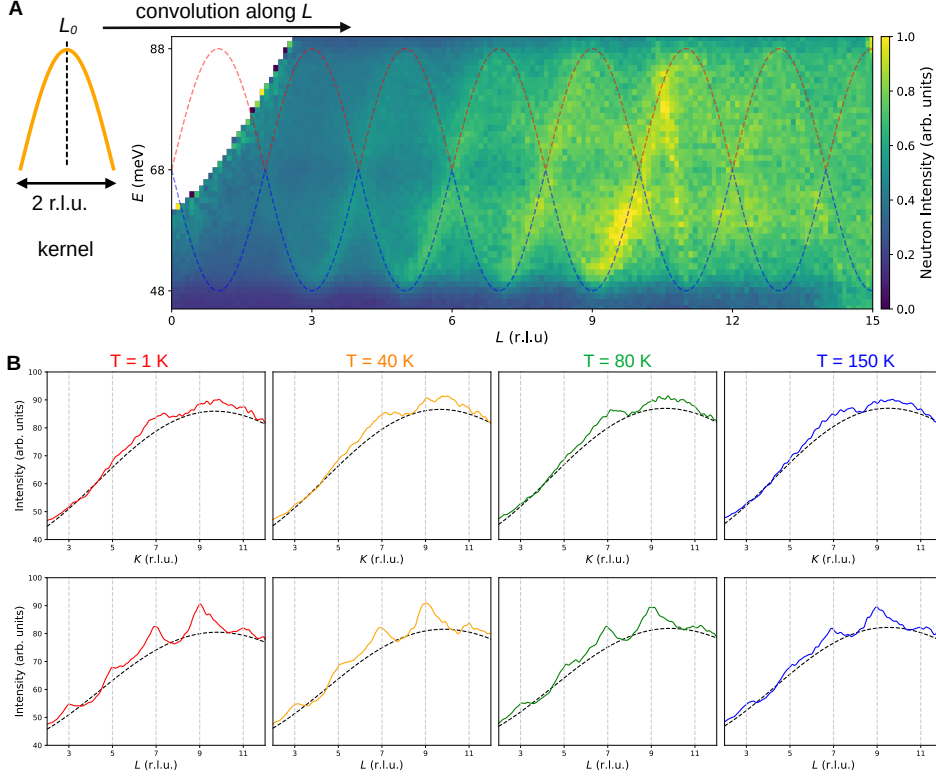


**Fig. 1 HDFL Phonon Intensities.** (A) INS intensities,  $I(L, E)$ , at 1 K, integrated over  $H$  and  $K$  in the range 0–4 r.l.u. The high- and low-frequency dispersive librational phonons are fitted with cosine functions, shown as red and blue dashed lines, respectively. The 1D HDL intensity,  $I(L)$ , is extracted by convolving  $I(L, E)$  with the cosine-shaped kernel shown in orange. (B)  $I(K)$  and  $I(L)$  at 1, 40, 80, and 150 K, with flat backgrounds indicated by black dashed lines.

be identified as the bending modes of  $^2\text{H}_2\text{O}$  and  $^1\text{H}_2\text{O}$ , respectively. Notably, no peak was observed at 185 meV, ruling out contributions from  $^1\text{HO}^2\text{H}$  bending modes. These findings strongly suggest that the impurity originates from polycrystalline  $^1\text{H}_2\text{O}$  frost forming on the sample surface during handling, rather than being intrinsic to the ice Ih structure.

The peak intensities at 150 meV ( $^2\text{H}_2\text{O}$  bending modes) and 200 meV ( $^1\text{H}_2\text{O}$  bending modes) are nearly equal (fig. 2). Considering these modes are mostly incoherent and the incoherent scattering cross-sections of  $^2\text{H}$  and  $^1\text{H}$  are 2.05 and 80.27 barn [20], respectively, the data suggest the  $^1\text{H}_2\text{O}$  frost contamination is 2-3%. However, this minor contamination does not affect the dispersive librational phonon features we observed because  $^1\text{H}$  has a small coherent scattering length, and its contribution to coherent scattering is negligible.

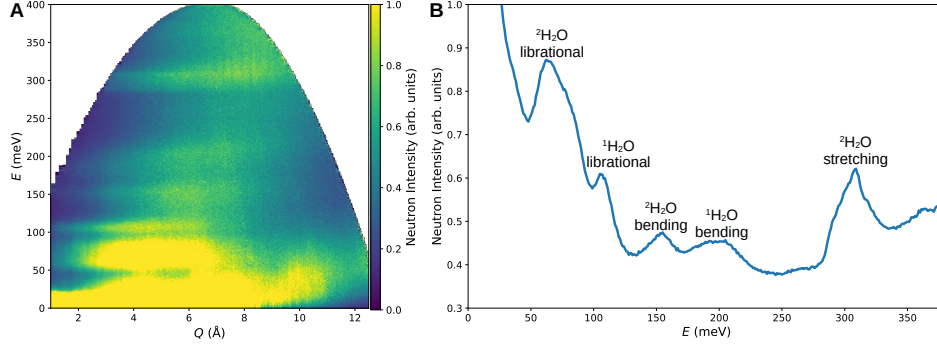


**Fig. 2 Phonon Intensities with  $E_i = 400$  meV.** (A) INS intensities,  $I(Q, E)$ , measured at 1 K with an incident energy of 400 meV. (B) Integrated INS intensities,  $I(E)$ . Peaks are identified as follows: 70 meV -  $^2\text{H}_2\text{O}$  librational modes, 105 meV -  $^1\text{H}_2\text{O}$  librational modes, 150 meV -  $^2\text{H}_2\text{O}$  bending modes, 200 meV -  $^1\text{H}_2\text{O}$  bending modes, and 310 meV -  $^2\text{H}_2\text{O}$  stretching modes.  $^1\text{H}_2\text{O}$  frost contamination is estimated as 2-3%.

## Force Constant Matrix

The force constant matrix (FCM),  $\Phi$ , is a key component in solving equations of motion for atoms in crystals, allowing for the calculation of the dynamic structure factor (DSF) to compare with INS data.

For an  $N$ -atom harmonic system,  $\Phi$  is an  $N \times N$  block matrix consisting of  $3 \times 3$  blocks  $\Phi_{ij}$  representing the second derivative of the potential energy  $U = \frac{1}{2} \sum_{i,j=1}^N \mathbf{u}_i^T \Phi_{ij} \mathbf{u}_j$ , where  $\mathbf{u}_i$  and  $\mathbf{u}_j$  are the atomic displacement vector of the  $i$ -th and  $j$ -th atom [31]. The system's dynamics are governed by the equation of motion  $\ddot{\mathbf{u}} = -\mathbf{M}^{-1} \Phi \mathbf{u}$ , where  $\mathbf{M}$  is the diagonal mass matrix. Solving this yields the atomic displacements  $\mathbf{u}_{\mathbf{q}\nu}(t) = A_{\mathbf{q}\nu} \mathbf{e}_{\mathbf{q}\nu} e^{i\omega_{\mathbf{q}\nu} t}$  with  $\mathbf{e}_{\mathbf{q}\nu}$  and  $\lambda_{\mathbf{q}\nu} = \omega_{\mathbf{q}\nu}^2$  being the  $\nu$ -th eigenvector and eigenvalue of  $\mathbf{M}^{-1} \Phi^{\mathbf{q}}$ . The phonon wavevector  $\mathbf{q}$  modifies the force constants as  $\Phi_{ij}^{\mathbf{q}} = \Phi_{ij} e^{i\mathbf{q} \cdot \mathbf{r}_{ij}}$ .

$\Phi$  can be calculated using density functional theory (DFT), but is problematic for ice Ih [45–47]; these calculations depend on hydrogen conformations, lack generality, may break conservation of angular momentum, and are computationally demanding.

## Stretching and Bending Interactions

We derived FCM of stretching and bending interactions by first defining  $\mathbf{r}_f$  and  $\mathbf{r}_g$  as two arbitrary vectors that are linear combinations of atomic coordinates  $\mathbf{r}_i$  ( $i = 1-N$ ):

$$\begin{bmatrix} \mathbf{r}_f \\ \mathbf{r}_g \end{bmatrix} = \begin{bmatrix} f_1 & \cdots & f_N \\ g_1 & \cdots & g_N \end{bmatrix} \begin{bmatrix} \mathbf{r}_1 \\ \vdots \\ \mathbf{r}_N \end{bmatrix}$$

so that  $\mathbf{u}_f = \Delta \mathbf{r}_f$  and  $\mathbf{u}_g = \Delta \mathbf{r}_g$  are linear combinations of atomic displacements  $\mathbf{u}_i$  ( $i = 1-N$ ):

$$\begin{bmatrix} \mathbf{u}_f \\ \mathbf{u}_g \end{bmatrix} = \begin{bmatrix} f_1 & \cdots & f_N \\ g_1 & \cdots & g_N \end{bmatrix} \begin{bmatrix} \mathbf{u}_1 \\ \vdots \\ \mathbf{u}_N \end{bmatrix}$$

For the stretching interactions, let  $\mathbf{r}_f$  be the vector of bond  $b$ :  $\mathbf{r}_f = \mathbf{b}$ ,  $\mathbf{u}_f = \Delta \mathbf{b}$ .  $\Delta \mathbf{b}$  can be decomposed into two components:  $\Delta \mathbf{b}^{\parallel}$ , which is parallel to  $\mathbf{b}$  and contributes to the stretching potential energy change, and  $\Delta \mathbf{b}^{\perp}$ , which is perpendicular to  $\mathbf{b}$  and only contributes to the reorientation of  $\mathbf{b}$ . The magnitude of the parallel component is given by  $|\Delta \mathbf{b}^{\parallel}| = \mathbf{u}_f \cdot \frac{\mathbf{r}_f}{r_f}$ . The stretching potential energy is:

$$U_b = \frac{1}{2} k_b |\Delta \mathbf{b}^{\parallel}|^2 = \frac{1}{2} k_b [\mathbf{u}_f^T] \begin{bmatrix} \mathbf{r}_f \mathbf{r}_f \\ r_f^2 \end{bmatrix} [\mathbf{u}_f]$$

The corresponding FCM is:

$$\Phi_{\mathbf{b}=\mathbf{r}_f} = k_b \begin{bmatrix} f_1 \\ \vdots \\ f_N \end{bmatrix} \begin{bmatrix} \mathbf{r}_f \mathbf{r}_f \\ r_f^2 \end{bmatrix} [f_1 \cdots f_N]$$

For the bending interactions, let  $\mathbf{r}_f$  and  $\mathbf{r}_g$  be the two vectors of angle  $\alpha$ , and  $\mathbf{n}$  be the unit vector perpendicular to both  $\mathbf{r}_f$  and  $\mathbf{r}_g$ :  $\mathbf{n} = \frac{\mathbf{r}_f \times \mathbf{r}_g}{|\mathbf{r}_f \times \mathbf{r}_g|}$ . In the case where  $\mathbf{r}_f \parallel \mathbf{r}_g$ ,  $\mathbf{n}$  can be any unit vector perpendicular to  $\mathbf{r}_f$ , and the final FCM should be an average over all possible  $\mathbf{n}$  (practically, we only need two vectors  $\mathbf{n}_1$  and  $\mathbf{n}_2$  that are perpendicular to each other). Define the angle vector  $\alpha = \alpha \mathbf{n}$ . The change in the angle vector is given by:  $\Delta \alpha = \mathbf{u}_f \times \frac{\mathbf{r}_f}{r_f} - \mathbf{u}_g \times \frac{\mathbf{r}_g}{r_g}$ .  $\Delta \alpha$  can be decomposed into two components:  $\Delta \alpha^{\parallel}$ , which is parallel to  $\mathbf{n}$  and contributes to the change in bending potential energy, and  $\Delta \alpha^{\perp}$ , which is perpendicular to  $\mathbf{n}$  and only contribute to the reorientation of  $\alpha$ . The parallel component is:

$$\Delta \alpha^{\parallel} = (\Delta \alpha) \cdot \mathbf{n} = \mathbf{u}_f \cdot \left( \frac{\mathbf{r}_f}{r_f} \times \mathbf{n} \right) - \mathbf{u}_g \cdot \left( \frac{\mathbf{r}_g}{r_g} \times \mathbf{n} \right)$$

If we define  $\mathbf{w}_f = \left( \frac{\mathbf{r}_f}{r_f} \times \mathbf{n} \right)$ ,  $\mathbf{w}_g = \left( \frac{\mathbf{r}_g}{r_g} \times \mathbf{n} \right)$ , then the bending potential energy is:

$$U_\alpha = \frac{1}{2} k_\alpha |\Delta \alpha^{\parallel}|^2 = \frac{1}{2} k_\alpha [\mathbf{u}_f^T \quad \mathbf{u}_g^T] \begin{bmatrix} \mathbf{w}_f \mathbf{w}_f & -\mathbf{w}_f \mathbf{w}_g \\ -\mathbf{w}_g \mathbf{w}_f & \mathbf{w}_g \mathbf{w}_g \end{bmatrix} \begin{bmatrix} \mathbf{u}_f \\ \mathbf{u}_g \end{bmatrix}$$

The corresponding FCM is:

$$\Phi_{\alpha=\angle(\mathbf{r}_f, \mathbf{r}_g)} = k_\alpha \begin{bmatrix} f_1 & g_1 \\ \vdots & \vdots \\ f_N & g_N \end{bmatrix} \begin{bmatrix} \mathbf{w}_f \mathbf{w}_f & -\mathbf{w}_f \mathbf{w}_g \\ -\mathbf{w}_g \mathbf{w}_f & \mathbf{w}_g \mathbf{w}_g \end{bmatrix} \begin{bmatrix} f_1 & \cdots & f_N \\ g_1 & \cdots & g_N \end{bmatrix}$$

## Force Constant Parameter Determination

We determined the FCM model parameters from MSC shown in Fig. 3b:

(1) The  $(3n+1)$ -th mode primarily depends on  $\omega_{\angle\text{OH-O}}$ , giving  $\hbar\omega_{\angle\text{OH-O}} \simeq \hbar\omega_{3n+1} = 48$  meV.

(2)  $\omega_{\angle\text{HO-H}}$  and  $\omega_{\angle\text{H-O-H}}$  affect the broadening of the LFL and HFL modes, respectively. Therefore, we estimate  $\hbar\omega_{\angle\text{HO-H}} \simeq \hbar\sqrt{\omega_{5n}^2 - \omega_{3n+1}^2} = 47$  meV and  $\hbar\omega_{\angle\text{H-O-H}} \simeq \hbar\sqrt{\omega_{6n}^2 - \omega_{3n+1}^2} = 74$  meV.

(3)  $\omega_{\text{O-H}}$  is highly correlated with  $\omega_{\text{OO}}$  for lattice modes and  $\omega_{\text{OH}}$  for stretching modes. To simplify, we manually set  $\omega_{\text{O-H}}$  to zero, effectively projecting its real values onto  $\omega_{\text{OH}}$  and  $\omega_{\text{OO}}$ .

(4) We estimate  $\hbar\omega_{\text{OH}} \simeq \text{mean}(\hbar\omega^{\text{stretch}}) = 310$  meV and  $\hbar\omega_{\angle\text{HOH}} \simeq \text{mean}(\hbar\omega^{\text{bend}}) = 150$  meV from INS measurement with 400 meV incident energy (fig. 2B).

Using these initial estimates, we fine-tuned the model parameters to match the full neutron data. The results are:  $\hbar(\omega_{\text{OH}}, \omega_{\text{OO}}, \omega_{\angle\text{OH-O}}, \omega_{\angle\text{HOH}}, \omega_{\angle\text{HO-H}}, \omega_{\angle\text{H-O-H}}) = (310, 26, 59, 150, 48, 66)$  meV.

## DSF Simulation of Multiple-phonon and One-phonon Processes

We simulated the DSF for coherent multiple-phonon emission using the formula[41]:

$$S(\mathbf{Q}, \omega) = \frac{k'N}{k} e^{-\langle |\mathbf{Q} \cdot \mathbf{u}|^2 \rangle} \sum_{\omega_{\mathbf{q}\nu} \leq \omega} \sum_{\mathbf{q}} \int_t \left| \sum_i \frac{\bar{b}_i}{\sqrt{2m_i\omega_{\mathbf{q}\nu}}} e^{i\mathbf{Q} \cdot (\mathbf{r}_i + \mathbf{u}_{\mathbf{q}\nu}^i(t))} \right|^2 (n_{\mathbf{q}\nu} + 1) dt$$

Where  $\mathbf{k}$  is the initial neutron wavevector,  $\mathbf{k}'$  is the final wavevector,  $\mathbf{Q} = \mathbf{k}' - \mathbf{k}$  is the momentum transfer,  $N$  is the number of atoms in the system. The Debye-Waller factor is given by  $e^{-\langle |\mathbf{Q} \cdot \mathbf{u}|^2 \rangle}$ . The summations are over the number of atoms  $j$ , phonon energy less than or equal to the neutron energy ( $\omega_{\mathbf{q}\nu} \leq \omega$ ), and phonon wavevector  $\mathbf{q}$ . The integration is over time  $t$ . The instantaneous atomic displacement is  $\mathbf{u}_{\mathbf{q}\nu}^i(t)$ , and  $n_{\mathbf{q}\nu}$  is the phonon number given by the Bose-Einstein distribution which approximately equals 1 at low temperature.

We simulated DSF for coherent one-phonon emission using the formula[41]:

$$S(\mathbf{Q}, \nu, \omega) = \frac{k'N}{k} e^{-\langle |\mathbf{Q} \cdot \mathbf{u}|^2 \rangle} \sum_{\mathbf{q}=\mathbf{Q}} \left| \sum_i \frac{\bar{b}_i}{\sqrt{2m_i\omega_{\mathbf{q}\nu}}} e^{i\mathbf{Q} \cdot \mathbf{r}_i} \mathbf{Q} \cdot \mathbf{e}_{\mathbf{q}\nu}^i \right|^2 (n_{\mathbf{q}\nu} + 1) \delta(\omega - \omega_{\mathbf{q}\nu})$$

$\mathbf{e}_{\mathbf{q}\nu}$  is the  $\nu$ -th phonon normal mode and  $\mathbf{e}_{\mathbf{q}\nu}^j$  is its component for the  $j$ -th atom. This is also known as the phonon polarization vector, whose direction is along which atoms vibrate, [31]. All simulations incorporate energy-dependent instrumental resolutions.

## Detailed Calculations of Conformational Entropy

In ice Ih, each hydrogen bond can adopt one of three possible bond types (fig. 4a), so the total number of hydrogen conformations is given by  $W = 3^{N_{\text{h}}}$  where  $N_{\text{h}}$  is the number of hydrogen bonds. For a specific set of values  $(\rho_0, \rho_3)$ , the number of

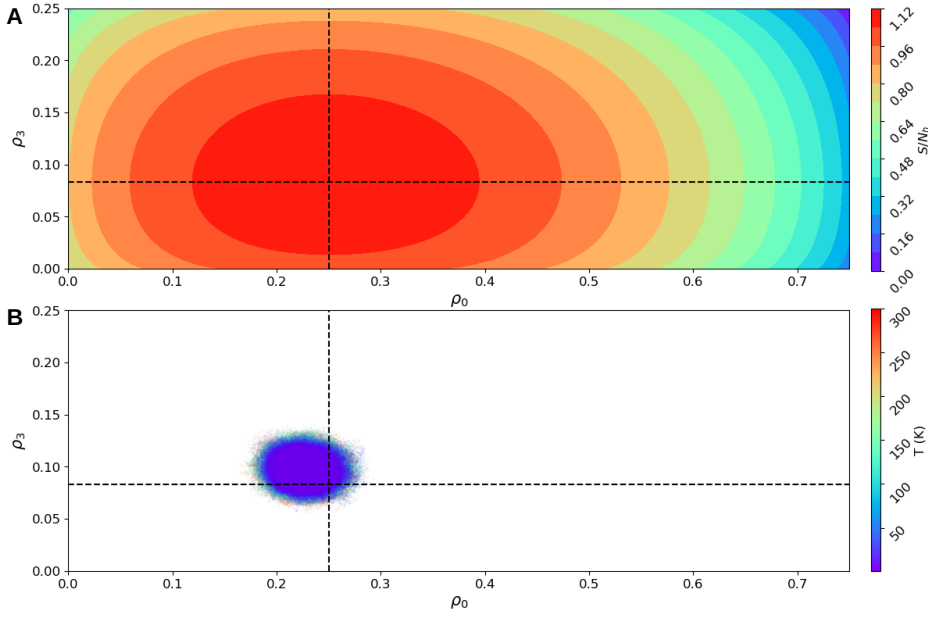


**Fig. 3 Entropy landscape and simulated annealing results in  $(\rho_0, \rho_3)$  plane.** (A) Contour plot of conformational entropy  $S(\rho_0, \rho_3)$  per hydrogen bond, showing regions of low and high entropy. (B) Simulated annealing results for a  $6 \times 3 \times 3$  supercell cooled from 300 K to 1 K, considering only dipole interactions without NNII. No clear formation of armchair or zigzag chains was observed.

conformations can be calculated as

$$W(\rho_0, \rho_3) = \binom{\frac{3}{4}N_h}{\rho_0 N_h} \cdot \binom{\frac{1}{4}N_h}{\rho_3 N_h} \cdot 2^{(1-\rho_0-\rho_3)N_h}$$

Using the approximation  $\log \binom{a}{b} \approx a \log a - b \log b - (a-b) \log(a-b)$ , we can derive the expression for the entropy per hydrogen bond:

$$\begin{aligned} \frac{1}{N_h} S(\rho_0, \rho_3) &= \frac{1}{N_h} \log W(\rho_0, \rho_3) \\ &\approx -\rho_0 \log \rho_0 - \left(\frac{3}{4} - \rho_0\right) \log\left(\frac{3}{4} - \rho_0\right) - \rho_3 \log \rho_3 - \left(\frac{1}{4} - \rho_3\right) \log\left(\frac{1}{4} - \rho_3\right) - (1 - \rho_0 - \rho_3) \log 2 \\ &= -\rho_0 \log \rho_0 - \rho_3 \log \rho_3 - \left(\frac{3}{4} - \rho_0\right) \log\left(\frac{3}{8} - \frac{1}{2}\rho_0\right) - \left(\frac{1}{4} - \rho_3\right) \log\left(\frac{1}{8} - \frac{1}{2}\rho_3\right) \end{aligned}$$

$\frac{1}{N_h} S(\rho_0, \rho_3)$  is plotted in fig. 3A.

## Structures of Local Entropy-Minimum Conformations

From the formula for conformational entropy, we see that  $S(\rho_0, \rho_3)$  reaches local minima at the four corners of the  $(\rho_0, \rho_3)$  plane, corresponding to four conformations: ice  $\text{Ih}^I$ ,  $\text{Ih}^{II}$ ,  $\text{Ih}^{III}$ , and  $\text{Ih}^{IV}$ . Typical crystal structures of these conformations are shown in fig. 4. The conformations of  $\text{Ih}^{II}$ ,  $\text{Ih}^{III}$ , and  $\text{Ih}^{IV}$  are not unique due to symmetry-equivalent hydrogen bonds where  $E_1 = E_4$  and  $E_2 = E_5$ .  $\text{Ih}^I$  consists of 50% armchair

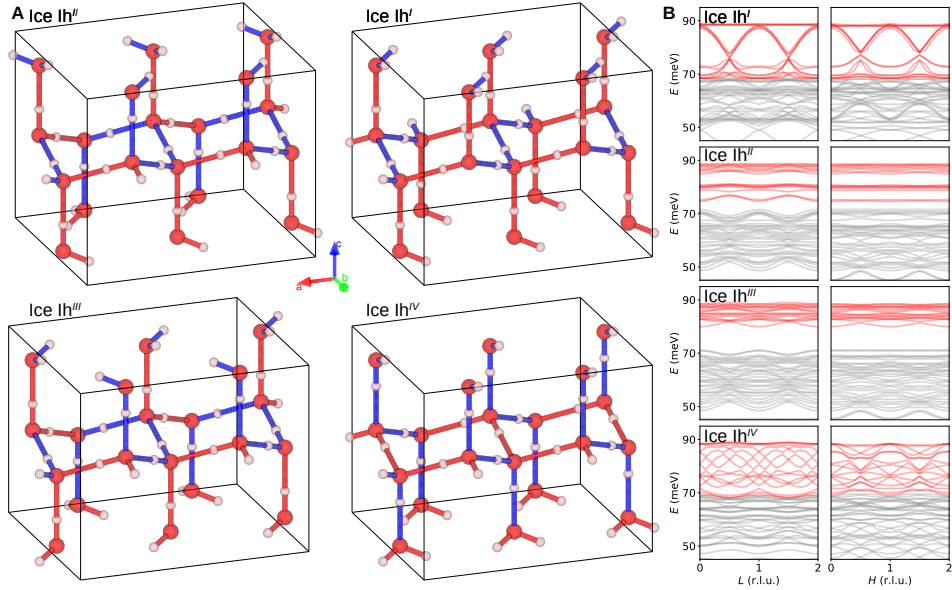


**Fig. 4 Crystal Structures and Phonon Band Structures of Ice  $Ih^I$ ,  $Ih^{II}$ ,  $Ih^{III}$ , and  $Ih^{IV}$ .** (A) Representative crystal structures of ice  $Ih^I$ ,  $Ih^{II}$ ,  $Ih^{III}$ , and  $Ih^{IV}$  displayed in  $2 \times 1 \times 1$  supercells. Positive and negative Ising chains are shown in red and blue, respectively. (B) Phonon band structures of ice  $Ih^I$ ,  $Ih^{II}$ ,  $Ih^{III}$ , and  $Ih^{IV}$  along the  $L$  and  $H$  directions.

chains (red) and 50% zigzag chains (blue);  $Ih^{II}$  consists entirely of arch chains (both red and blue);  $Ih^{III}$  consists entirely of spiral chains (both red and blue); and  $Ih^{IV}$  consists of 50% step chains (blue) and 50% zigzag chains (red).

Phonon band structures along the  $L$  and  $H$  directions are shown in fig. 4B where LFL modes are plotted in grey, and HFDL modes in red. We see that armchair and zigzag chains are the only Ising chains that can generate HFDL phonon bands long along the  $L$  and  $H$  directions, respectively, consistent with our prior discussions.

### Derivation of Zigzag and Armchair Chain Densities

Armchair chains contain 50% type-0 bonds and 50% type-3 bonds whereas zigzag chains contain 100% type-0 bonds, as shown in Fig. 4b. Starting from the fully ordered ice XI structure, where the system consists of 50% armchair chains and 50% zigzag chains, i.e.  $(\rho_z, \rho_a) = (\frac{1}{2}, \frac{1}{2})$ , annealing a zigzag chain with  $\delta\rho_z N_{OO}$  hydrogen bonds (effectively converting type-0 bonds to a random mixture of type-0, 2, 4 bonds, and type-3 bonds to a random mixture of type-1, 3, 5 bonds) will reduce  $(\rho_0, \rho_3)$  by  $(\frac{2}{3}\delta\rho_z, 0)$ . Similarly, annealing an armchair chain with  $\delta\rho_a N_{OO}$  hydrogen bonds will reduce  $(\rho_0, \rho_3)$  by  $(\frac{1}{3}\delta\rho_a, \frac{1}{3}\delta\rho_a)$ . Thus, we have  $(\delta\rho_0, \delta\rho_3) = (\frac{2}{3}\delta\rho_z + \frac{1}{3}\delta\rho_a, \frac{1}{3}\delta\rho_a)$ .

Using the ice XI conformation as an initial condition, where  $(\rho_z, \rho_a, \rho_0, \rho_3)_{\text{ice XI}} = (\frac{1}{2}, \frac{1}{2}, \frac{3}{4}, \frac{1}{4})$ , we can subtract these values into the equation and solve for  $(\rho_z, \rho_a) - (\frac{1}{4}, \frac{1}{12}) = (\frac{2}{3}\rho_z + \frac{1}{3}\rho_a, \frac{1}{3}\rho_a)$ . The solution yields  $\rho_a = 3\rho_3 - \frac{1}{4}$  and  $\rho_z = \frac{3}{2}(\rho_0 - \rho_3) - \frac{1}{4}$ .

This solution predicts that at the highest-entropy conformation, where  $(\rho_0, \rho_3) = (\frac{1}{4}, \frac{1}{12})$ , the resulting chain densities are  $(\rho_z, \rho_a) = (0, 0)$ . At this conformation, corresponding to infinite temperature where entropy dominates over energy, the partial order vanishes, and the system contains no zigzag or armchair chains. This result is consistent with our mechanism that partial order is driven by NNII.

The experimentally observed HFDL phonon densities,  $\rho_K(T)$  and  $\rho_L(T)$ , are proportional to  $\rho_z(T)$  and  $\rho_a(T)$ , respectively, under the assumption that the average lengths of the zigzag and armchair chains remain constant. However, this relationship is sensitive to the chain lengths. Shorter zigzag or armchair chains will significantly reduce the HFDL phonon densities observed experimentally because the vibrational modes associated with these chains become localized.

## Details of Simulated Annealing Methods

We used simulated annealing algorithm to simulate the evolution of the hydrogen conformation at finite temperature. We generated a random  $6 \times 3 \times 3$  supercell ice Ih structure whose hydrogen conformation obeys the ice rules. Temperature is set to decrease linearly from 300 K to 1 K with 200,000 steps. A neighboring state is generated by identifying one of the "OH-OH-OH-..." loops (typically containing 6 to 8 hydrogen atoms) within the structure and flipping all the Ising variables of the hydrogen atoms along the loop. This method ensures that the new structure still obeys the ice rules while minimizing the difference from the previous state. For each state, the internal energy  $U(\rho_0, \rho_3)$  is calculated. The decision to accept or reject the new state is based on the Metropolis criterion, where the acceptance probability is 1 when  $\Delta U < 0$  and  $\exp(-\Delta U/T)$  when  $\Delta U > 0$ .

Simulated annealing results considering only dipole interactions without NNII are shown in fig. 4B. No clear formation of armchair or zigzag chains was observed.

## End Notes

**Acknowledgements.** We wish to thank Rick Goyette, Saad Elorfi, Qiang Zhang, Nathan C Helton, Randall Sexton, Scott Tidwell, Robert Marrs, Chyan Duncan, Gary Lynn, Bobby Cross Jr., Andrew Parizzi, Silbino Vasquez, Douglas Engle, Colin Sarkis, Christian Balz, Alex Koldys (ORNL), Stephen Mills and Justin Link (Xavier University) for help with the sample handling and logisites. We wish to thank Takeshi Egami for insightful discussions.

A portion of this research used resources at the Spallation Neutron Source, a DOE Office of Science User Facility operated by the Oak Ridge National Laboratory. The beam time was allocated to CORELLI and ARCS on proposal number IPTS-22517.1 and IPTS-33330.1.

**Funding.** We acknowledge financial support by the Helmholtz Association of German Research Centers as well as Deutsche Forschungsgemeinschaft under Grants No.

SFB 1143 and No. EXC 2147 ct.qmat. Travel funds for D.J.P.M. and J.L. were provided by the John Hauck Foundation and the Xavier University College of Arts and Sciences. The work of T.C. and D.A.T. was aided by the University of Tennessee Materials Research Science & Engineering Center – The Center for Advanced Materials and Manufacturing – supported by the National Science Foundation under DMR No. 2309083.

**Competing interests.** The authors have no competing interests.

**Data availability.** All data, simulation outputs, and materials underlying this study will be made publicly accessible at the time of publication to enable reproduction of the results presented. Data and code will be deposited in a publicly accessible non-profit online repository that issues a DOI, with the specific repository and accession details to be confirmed prior to publication.

**Author contribution.** D.A.T., A.S., and D.J.P.M. designed and supervised the project. K.S., B.K., and D.J.P.M. prepared the samples. D.J.P.M., A.S., T.C., I.C.O., A.B., J.Y., J.L., and D.A.T. performed the neutron experiments. T.C. and A.S. analyzed the data. T.C. designed the model and performed the simulations. K.S., B.K., A.B., F.Y., D.L.A., and Z.J.M. provided resources. T.C., A.S., and Z.J.M. developed the software. T.C. wrote the manuscript and produced the figures with input from D.J.P.M., I.C.O., and D.A.T. All authors contributed to the manuscript and approved the final version. The paper reflects the contributions of all authors.

**Corresponding author.** Correspondence and requests for materials should be addressed to T.C. and D.A.T.

**Reprints.** Reprints and permissions information is available at [www.nature.com/reprints](http://www.nature.com/reprints).